ELSEVIER

Topographic modeling of Phoebe using Cassini images

Bernd Giese[a],*, Gerhard Neukum[b], Thomas Roatsch[a], Tilmann Denk[b], Carolyn C. Porco[c]

[a]*DLR-Institute of Planetary Research, Rutherfordst 2, 12489 Berlin, Germany*
[b]*Institut für Geologische Wissenschaften, Freie Universität, 12249 Berlin, Germany*
[c]*CICLOPS, Space Science Institute, 4750 Walnut Street, Boulder, CO 80301, USA*

Abstract

High-resolution Cassini stereo images of Saturn's moon Phoebe have been used to derive a regional digital terrain model (DTM) and an orthoimage mosaic of the surface. For DTM-control a network of 130 points measured in 14 images (70–390 m/pixel resolution) was established which was simultaneously used to determine the orientation of the spin-axis. The J2000 spin-axis was found at Dec $= 78.0° \pm 0.1°$ and RA $= 356.6° \pm 0.3°$, substantially different from the former Voyager solution. The control points yield a mean figure radius of 107.2 km with RMS residuals of 6.2 km demonstrating the irregular shape of this body. The DTM was computed from densely spaced conjugate image points determined by methods of digital image correlation. It has a horizontal resolution of 1–2 km and vertical accuracies in the range 50–100 m. It is limited in coverage, but higher in resolution than the previously derived global shape model of Phoebe [Porco et al., 2005. Cassini imaging science: initial results on Phoebe and Iapetus. Science 307, 1237–1242] and allows us to study the morphology of the surface in more detail. There is evidence for unconsolidated material from a steep and smooth slope at the rim of a 100 km impact feature. There are several conically shaped craters on Phoebe, which may hint at highly porous and low compaction material on the surface.
© 2006 Elsevier Ltd. All rights reserved.

Keywords: Phoebe; Cassini; Topographic mapping; Digital terrain model; Craters

1. Introduction

Phoebe is the outermost large satellite of Saturn. It moves in a retrograde orbit and is therefore believed to be a captured object (Pollack et al., 1979; Cuk and Burns, 2004). Unlike its neighbors, Phoebe is not tidally locked in its orbit. Rather, it revolves about Saturn in 550 days and spins at a rate of 9.3 h (Bauer et al., 2004). From the analysis of Voyager images obtained early in 1981, a rough spin-axis orientation (Colvin et al., 1989) and global shape parameters (diameters: $230 \times 220 \times 210$ km, Thomas et al., 1986) could be derived. However, poor image resolutions (best resolution 22 km/lp) have prevented detailed morphologic studies of the surface.

During Cassini's encounter with Phoebe on 11 June 2004, the imaging science subsystem (ISS) on board acquired a series of images with resolutions much improved over the early Voyager data. In a first analysis of the images, we derived a new spin-pole solution as well as a $2° \times 2°$ global shape model showing the major topographic landforms of Phoebe (Porco et al., 2005). However, about one half of Phoebe's surface was covered with high-resolution images to better than 200 m/pixel. These images provide multi-stereo coverage suitable for topographic mapping at substantially higher level of detail than revealed by the global shape model.

In this paper, we present the results of a photogrammetric analysis of the high-resolution stereo images involving a revisit of the spin-pole analysis, a regional digital terrain model (DTM) of the surface, and a DTM-based orthoimage mosaic. With the DTM in hand, we describe the morphology of craters and discuss implications.

2. Data base

The Cassini ISS consists of two framing cameras, a wide angle camera (WAC) and a narrow angle camera (NAC)

*Corresponding author. Tel.: +49 30 67055 322; fax: +49 30 67055 402.
E-mail address:* bernd.giese@dlr.de (B. Giese).

(Table 1), each equipped with a large number of spectral filters (Porco et al., 2004). The analysis of Phoebe images carried out in this paper involved 12 NAC and 2 WAC frames (Table 2) selected from imaging sequences taken prior to and after closest approach (range = 2175 km). During the acquisition of these frames the sub-spacecraft longitude changed by 119° (Table 2, col. #3), an indication for the high stereo potential of the data set. Unfortunately, the phase angles (Table 2, col. #4) reveal that for most of the images significant areas of Phoebe were in shadow and therefore exempt from modeling. Moreover, the two WAC frames suffer from substantial over-exposure (Fig. 1) but were nevertheless included in the analysis to maximize DTM coverage. The NAC frames are clear filter images and the WAC frames are a filter combination of clear and green. All frames were obtained within a lossless compression mode.

Spacecraft orbit and camera pointing data were taken from NAIF-SPICE kernels provided by the Cassini flight project.

3. Photogrammetric analysis

3.1. Least-squares adjustment

Terrain modeling at the stage of ground point calculations requires precise orbit- and camera pointing data close to the image resolutions and the instantaneous field of view of a pixel, respectively. But usually the spacecraft orbit has offset errors in the order of a kilometer or less, and nominal pointing errors are typically tens of pixels or even hundreds of pixels. Therefore, these errors must be corrected first. Moreover, the calculation of ground points is indirectly related to the body's rotational parameters, which may also be incorrect. To handle these problems, least-squares adjustment techniques using control points can be applied (Giese et al., 1998).

The observational data in the adjustment for Phoebe consist of the image coordinates of 130 control points (shown for two of the frames in Fig. 1) and the nominal camera pointing angles for the 14 images (see Table 2 for point statistics). Measurements of Phoebe's center of figure (assumed to represent the body's center of mass) were also made. Image points measured in NAC frames were extracted at an accuracy of 0.5 pixels and those measured in the WAC frames were considered to be accurate within 1 pixel only. For measurements of the center of figure, which were carried out by limb fitting, we adopted errors of 2 pixels. The nominal camera pointing data were assumed to be accurate within 1 mrad (Porco et al., 2004).

We considered the ground coordinates of the control points and the camera pointing angles as unknowns in the adjustment model. The spacecraft orbit was fixed, as there is not sufficient control information to correct the (minor) orbit errors and the pointing errors at the same time. While we made an attempt to estimate the rotational axis orientation of Phoebe, we anticipate that its rotational rate (which was recently re-determined by Bauer et al. (2004)) cannot be improved by our measurements.

In the technical realization of the least-squares adjustment software, the analysis is performed in the body-fixed frame. Thus, the rotational axis of Phoebe cannot be estimated directly but is incorporated in the conversion of the spacecraft positions and the camera pointing angles from the inertial J2000 frame to the Phoebe-fixed frame. Hence, in order to obtain a spin-axis solution for Phoebe coordinate conversion and least-squares adjustment were carried out repeatedly until a minimum misfit between the observations and the predicted values (RMS of the residuals) was achieved.

3.2. Results of the least-squares adjustment

Normalized misfits for the north pole declination and right ascension of Phoebe are given in Fig. 2. It shows that the pole declination is well constrained at $78.0° \pm 0.1°$ and differs from the former Voyager value by 11.3°. The right ascension is less constrained at $356.6° \pm 0.3°$ and closer to the Voyager result. Within the error limits, this spin pole solution agrees with the solution we obtained earlier within the framework of global shape modeling (Dec = 77.9°, RA = 356.6°; Porco et al., 2005).

Although the main purpose of the least-squares adjustment was to obtain improved camera pointing data for the

Table 1
ISS camera parameters used in the modeling

	NAC	WAC
Sensor	CCD framing cameras (1024 × 1024 pixels)	
Pixel size (mm)	0.012	0.012
Focal length (mm)	2003.44	200.77
FOV center (pixel)	512.5	512.5
Radial distortion	0	0

Table 2
Phoebe-stereo images involved in the analysis

Frame	Res (m)	s/c long (deg)	Phase (deg)	ctrl #
N1465664794	390	63	85	20
N1465668387	254	26	85	53
N1465669778	201	11	84	48
N1465669953	194	10	84	74
N1465672687	91	345	80	20
N1465672842	85	344	79	19
N1465672905	83	343	79	29
N1465673021	78	342	79	43
N1465673138	74	342	78	28
W1465674502	243	348	59	51
W1465674830	151	9	39	51
N1465677386	89	97	85	16
N1465677447	91	97	85	26
N1465679337	162	80	89	35

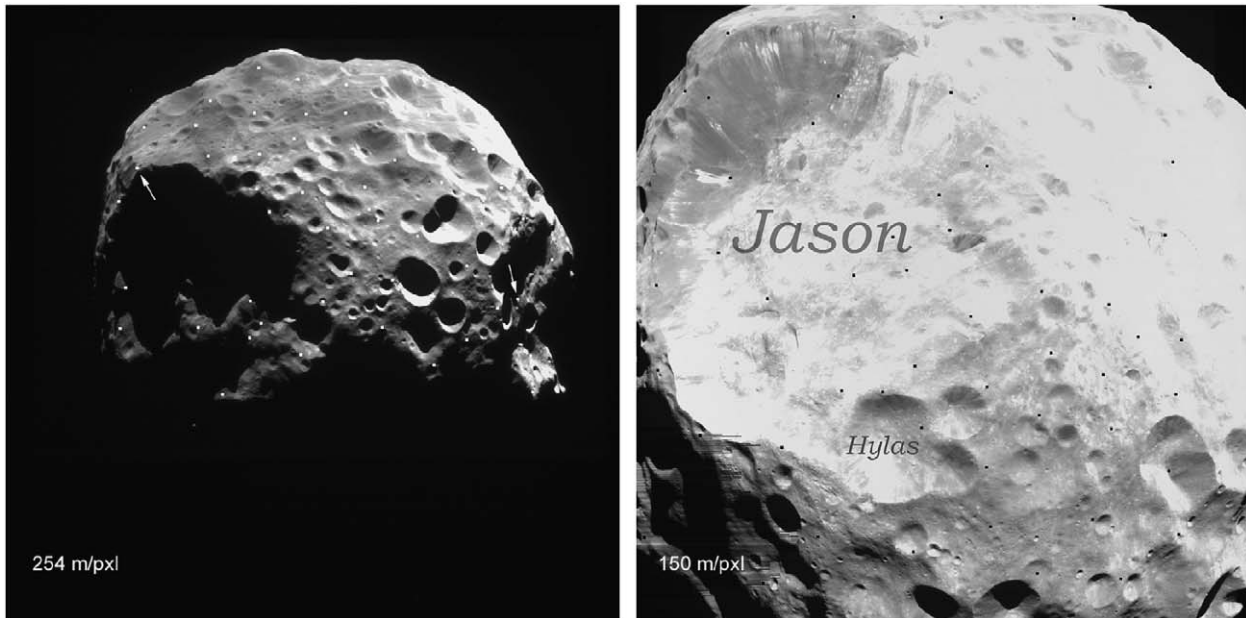Res: image resolution; ctrl: measured # of control points.

Fig. 1. Two of the frames used in the modeling: NAC frame N1465668387 (left) and WAC frame W1465674830 (right). Significant surface portions of Phoebe are in shadow (left, phase angle $= 85°$), and large parts of the WAC frame are saturated. Dots mark the locations of control points measured in the images, and arrows (left image) show the location of the highest (left) and lowest (right) point within the modeled area (Chapter 3.2). North is about to the left.
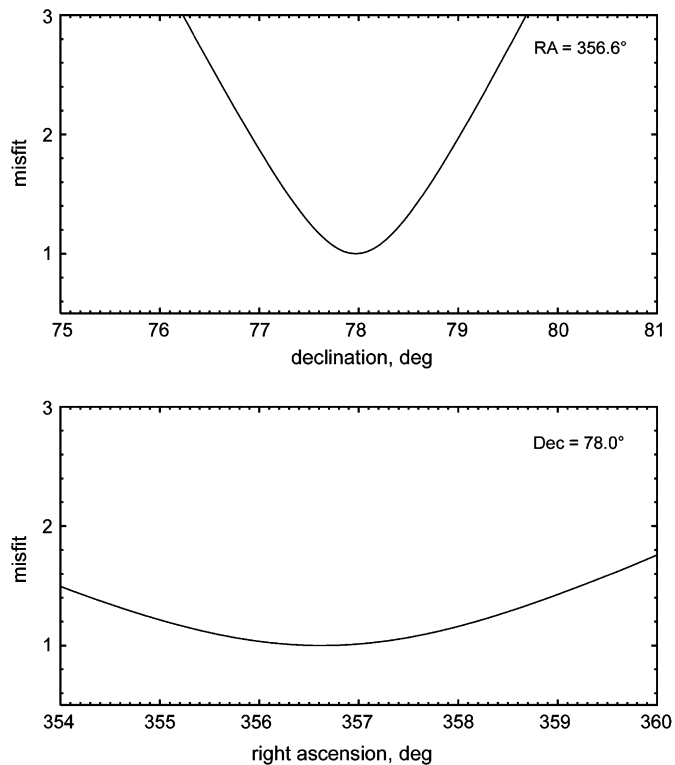

Fig. 2. Normalized misfits in dependence on spin pole- declination and right ascension. The former Voyager values are at $68.7°$ (declination) and $355.0°$ (right ascension), respectively.

Fig. 3. Control point locations (latitude, longitude) in a sinusoidal map projection.

1σ-accuracies in the x, y, and z coordinates are 279, 166, and 128 m, respectively, which is at the level of the image resolutions (Table 2). From these points the mean figure radius results in 107.2 km with RMS residuals of 6.2 km. Within the modeled area, the control point with the lowest elevation is located close to the south pole, 14.2 km below the mean figure, and the highest point can be found on the rim of the Jason impact crater (Fig. 1), 17.4 km above the mean sphere.

3.3. DTM generation

For the DTM generation, we determined large numbers of densely spaced conjugate points in the stereo images, using methods of digital image correlation (Wewel, 1996). Corresponding ground points were calculated by use of the

terrain modeling, it is very instructive to inspect the resulting control point coordinates, locations, and accuracies. The control points cover about 1/3 of the total surface including the south pole of Phoebe (Fig. 3). Their average
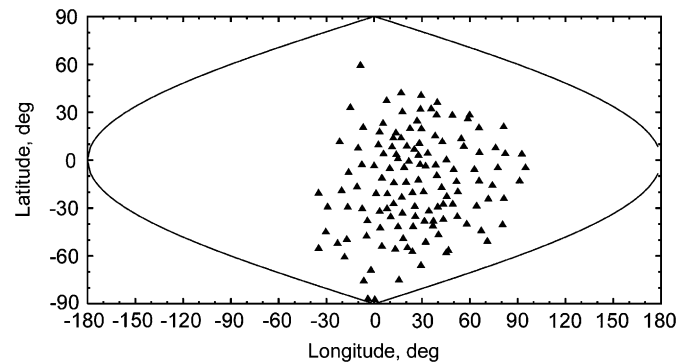
corrected camera pointing data from the least-squares adjustment and referenced to a sphere. Next, latitudes and longitudes of the points were converted into an ortho-graphic map projection, from which a contiguous DTM was interpolated. The final DTM was obtained by mosaicking of eight separate DTMs each generated from individual stereo pairs (Fig. 4). The DTM's horizontal resolution is in the range 1–2 km, and the vertical
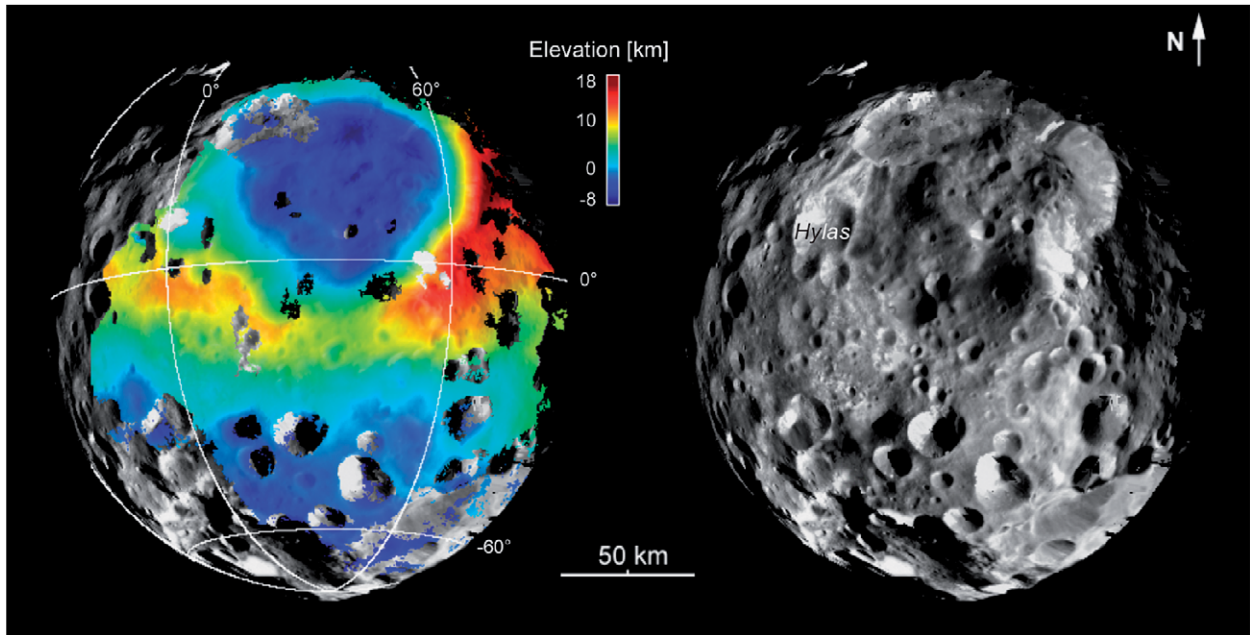

Fig. 4. Phoebe-DTM superimposed on ortho-rectified image data in an orthographic map projection (center latitude/longitude = 10°S/35°E). Elevations are given relative to a sphere of $R = 107$ km. In those areas not covered by the DTM the image data were rectified with respect to the reference sphere (Chapter 3.4).
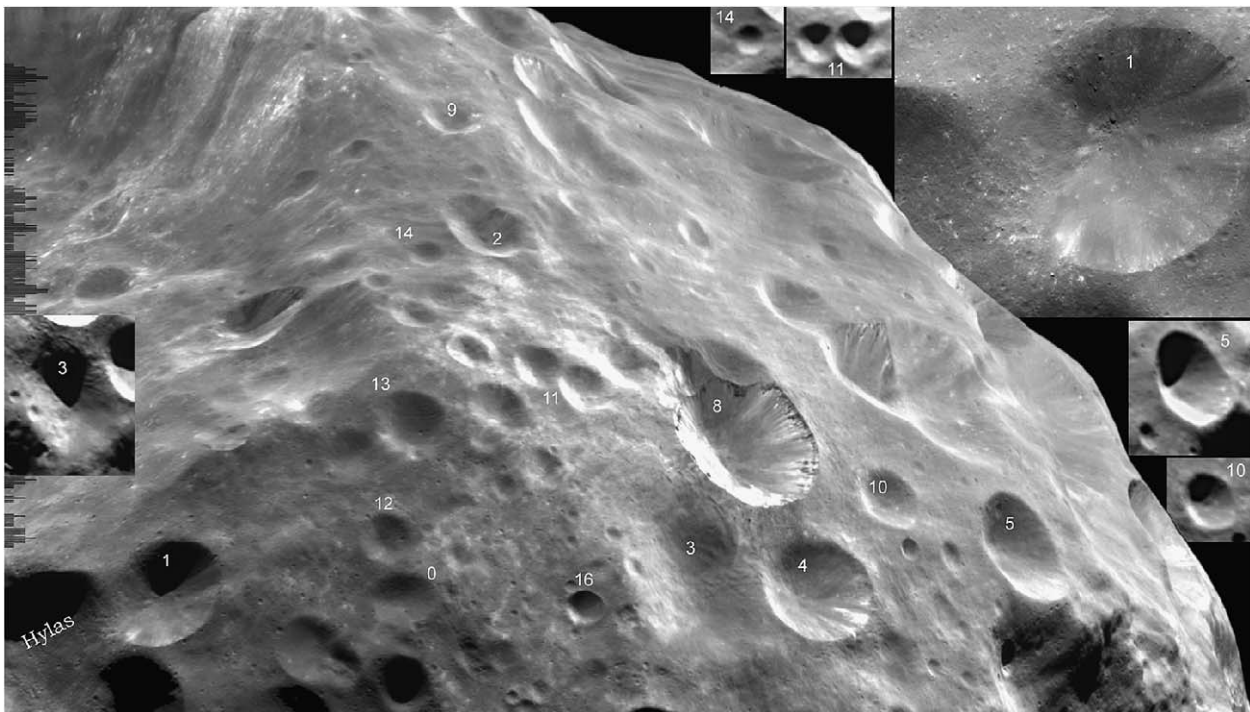

Fig. 5. Mosaic of N1465673021 and N1465672905 showing the morphology of craters on Phoebe. North is about to the left. For scaling, the diameter of crater #1 is 13 km. Apart from Jason (its southern rim runs along the line 1-13-14) all craters show simple morphologies. Exceptional is the conical shape of craters notably #1, which is shown at 18 m/pixel resolution (N1465674693). Conical craters can be distinguished from bowl-shaped craters by their cast shadows (Fig. 10). Potentially conical craters are # 1, 3, 5, 10, 11, (12), a potentially bowl-shaped crater is #14 but #13 may be too. Small insets (# 3, 5, 10, 11, 14) are cutouts of N1465669953.

accuracies reach 50–100 m, depending on topography and image contrast. Gaps in the DTM arise from areas where the image correlations failed, in particular areas with poor contrast such as shadows or over-exposed image portions (Fig. 1).

3.4. Orthoimages

With the terrain model available it is possible to ortho-rectify the images. Here, the image pixels are referenced to latitudes and longitudes by using the ray-intersection points with the terrain rather than the projection sphere. Thus, these orthoimages are free of parallaxes and suited for the production of geometrically correct image maps. Fig. 4 shows a mosaic of five orthoimages that perfectly match to each other and with the DTM. Unlike in maps produced without topographic information (Roatsch et al., this issue) there is no misregistration between the images and thus no further efforts for geometric corrections have to be taken.

3.5. Heights

The derived DTM uses a sphere as reference for heights and is therefore a radius model of the surface. This is convenient e.g. for photometric studies, which need the surface normals to compute the illumination- and observational angles. However, for studies of surface processes like e.g. mass movements heights measured relative to an equipotential surface or "dynamic heights" (Thomas, 1993) are required. Owing to the irregular shape of small satellites and rotational effects dynamic heights may differ substantially from spherical heights (Thomas, 1989, 1993). But for Phoebe, these differences are expected to be moderate (see Appendix). Therefore, in the morphologic analysis we will use the radius model rather than a dynamic

height model, and modifications are discussed when important.

4. Craters

With the obtained DTM we can now study the morphology of craters on Phoebe in detail. Craters are probes into the target and may give us information on the physical properties of the material.

4.1. Observations

A visual inspection of the images reveals that Phoebe basically exhibits simple crater shapes (Fig. 5). Complex morphologies including e.g. wall slumping or flat floors are not observed. The only exception is Jason, an impact crater with a diameter of ∼100 km (Fig. 1). The crater is shallow with respect to the outer topographic level and the floor is flat. Jason has a pronounced asymmetry in its rim heights and slopes. The eastern rim is much higher and steeper than the other rim sections (Fig. 4, 6). However, when corrections due to the rim topography (see Appendix) are taken into account the asymmetry becomes less pronounced but still remains (Fig. 6). The steepest slopes at the eastern rim then range from 35° to 40° only. This fits to the maximum slope inferred from the (dynamic heights) global shape model. While impact degradation has strongly modified most parts of Jason's rim, the eastern rim and slope are less degraded and appear to be well preserved. The rim is sharp and there are almost no craters visible on the slope (Fig. 7). There is no indication of wall slumping. Rather, the slope is smooth and constant to remarkable extent from top to bottom (Fig. 6; p3, p3′, p4). There is indication for large-scale landslides from bright streamers on the slope (Fig. 7).
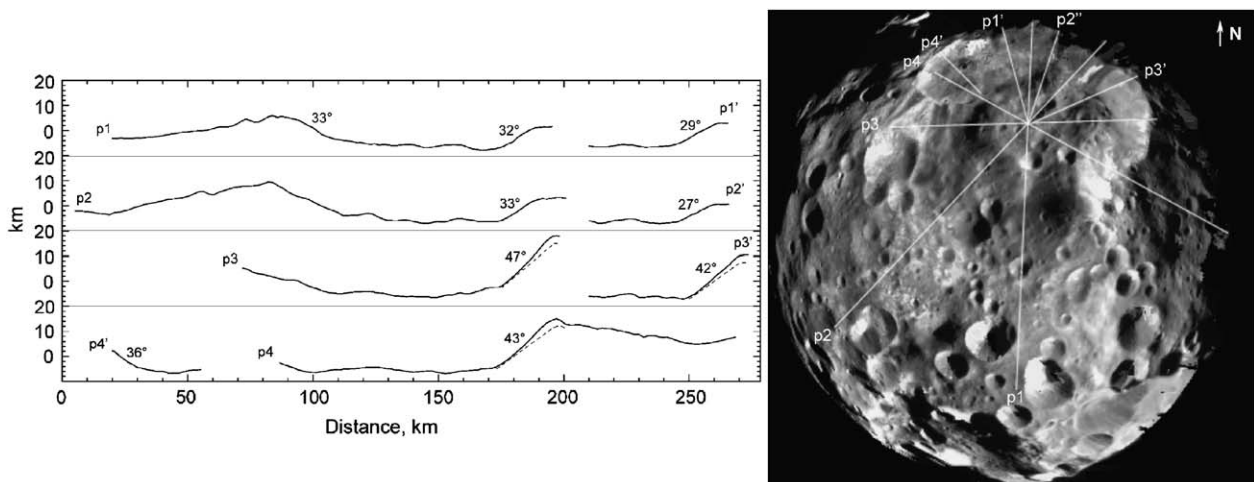

Fig. 6. Morphology of Jason impact crater. Note the large relief and steep slopes of the eastern crater wall. Dashed lines mark expected heights and slopes if measured relative to an equipotential surface (see Appendix). Profiles are not exaggerated.

Hylas is another prominent impact crater with asymmetric topography (Fig. 4). The crater walls have slopes in the range 33–37°, and there is a regional slope across the crater (Fig. 8). A smooth talus fan with a slope of ~34° is running into the crater. The depth-to-diameter ratio is 1:6.

In contrast to Hylas, all of the smaller-scale craters in the studied area have depth-to-diameter ratios above 1:6 (Fig. 9). Some of these show simple bowl-shapes (p7, p8) but most of the craters exhibit unusual conical shapes (p0–p6, p9). Their walls are tapered and the floor area is small. The depth-to-diameter ratios are typically above 1:5. As for the eastern rim of Jason, the wall slopes are smooth.

More, potentially conical craters can be identified by their characteristic cast shadows. While bowl-shaped craters result in broad more circular shadow contours conical craters show narrower parabolic shadow contours at specific illumination (Fig. 10). Examples are shown in Fig. 5 and Fig. 7. Conically shaped craters seem to dominate within the modeled area.

4.2. Implications

The shallowness of Jason is to some extent the result of landslides observed in several places along the rim (Fig. 7),
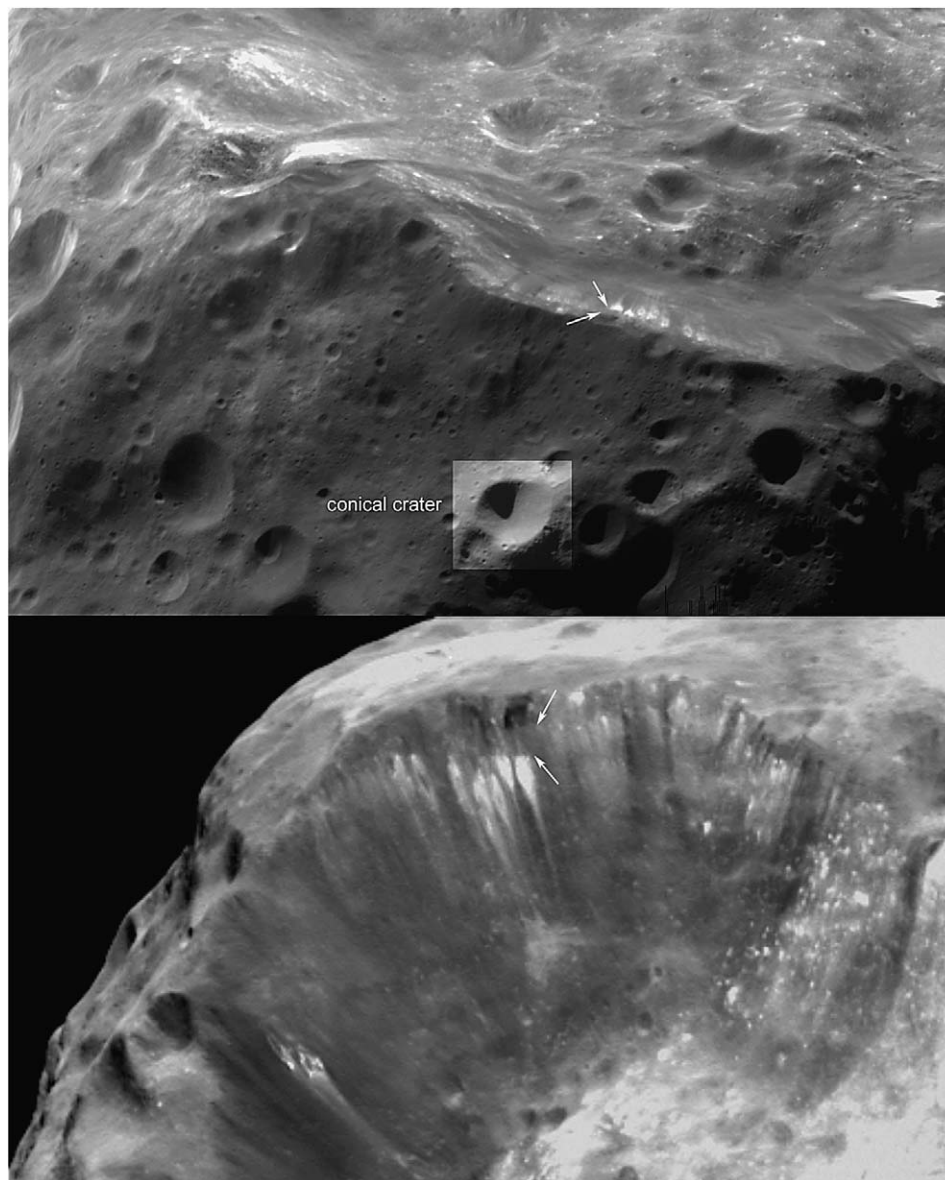

Fig. 7. (Top) Cutout of frame N1465677447 showing the eastern rim and part of the southern rim of Jason. The eastern rim is comparatively less impact degraded and appears to be fresh. (Bottom) Cutout of frame W1465674830 showing a front view of the eastern crater wall. Streamers visible in both views point to landslides. There is indication for layering (arrows) but without a topographic expression at the DTM's resolution. The slope is remarkably smooth and lacks features of wall slumping.
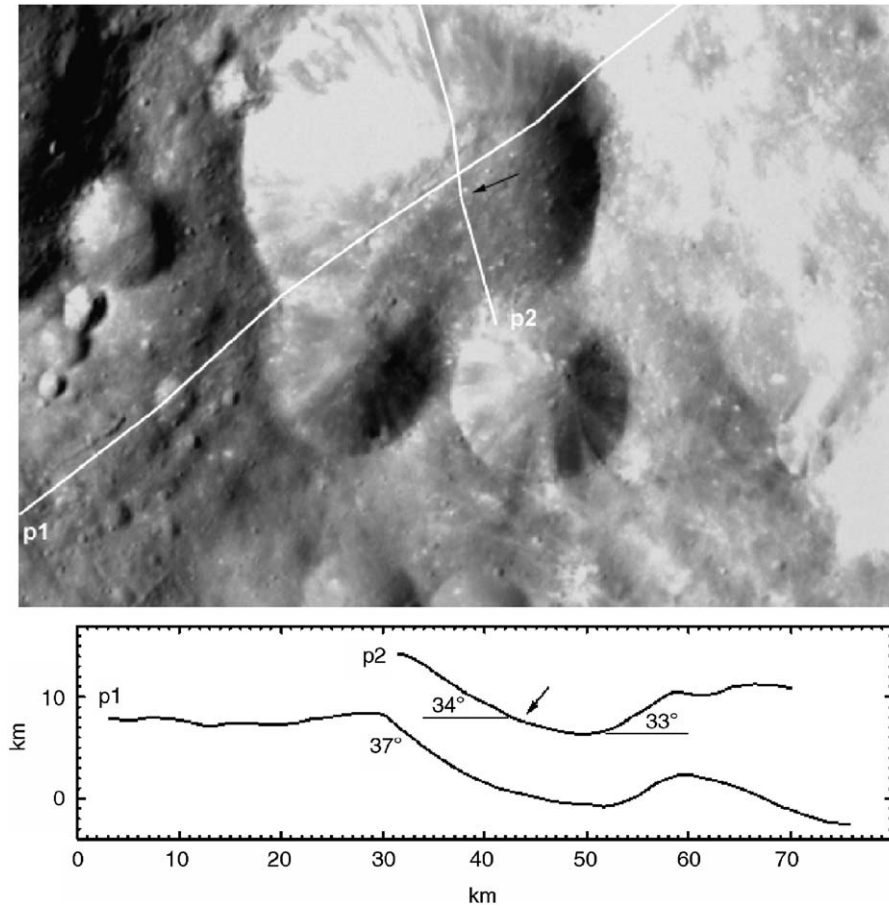
Fig. 8. Cutout of frame W1465674830 (North is about up) showing the morphology of the 28 km impact crater Hylas. The profiles reveal an asymmetric shape of Hylas. The arrow marks a small change in slope at the termination of a talus fan.

but the additional flatness of the floor suggests that both the shallowness and flatness basically have formed promptly at the time of impact. Viscous relaxation of the crater floor can be excluded because the expected temperatures at depth are too low for such a process. The asymmetry in relief of the crater walls may be related to an oblique impact or, alternatively, could be due to pre-existing regional topography. The presence of a smooth steep slope with obvious landslides on the eastern wall of Jason implies that it is a talus slope formed in unconsolidated material. Observed slopes of 35–40° might represent the range covered by the angle of repose for this material. The broad range may be related to different material properties (there is indication for layering, Fig. 7). On Earth, the angle of repose is typically 25–35° for sands (Herrmann, 2002) but higher slope angles are possible depending on properties like particle roughness, particle shape and size distribution (Robinson and Friedman, 2002; Zhou et al., 2002). In particular, coarse grains or small grains form steeper slopes than rounded grains or large grains. This may also hold for the ice grains on Phoebe, however, nothing is known about the nature of the ice grains and it is also plausible that marginal cohesion forces exist, which support a higher slope. The fresh appearance

of Jason's eastern rim and slope suggests that the last landslide may have occurred recently.

The asymmetric shape and regional slope across Hylas are obviously related to its location on the rim of Jason. The observed smooth talus fan further hints at unconsolidated material.

Lunar orbiter images reveal that conically shaped craters likely exist on the Earth's moon too (Fig. 10). This suggests that the formation of such craters cannot be related solely to the low-gravity environment or to the icy material on the surface of Phoebe. Explosion experiments show that such craters form in low-compaction material like loose dry sand (Piekutowski, 1977). A similar line of evidence comes from impact experiments performed to study cratering on asteroid Mathilde (Housen et al., 1999). Within these experiments, high-velocity impacts into porous, low-compaction material were carried out. Housen et al. (1999) obtained a conically shaped crater (#1642 in that paper) with a depth-to-diameter ratio of 1:3.8, close to what we have observed on Phoebe (crater #1). Hence, the conical craters on Phoebe may hint at highly porous and low-compaction target material, as has been presumed by Johnson and Lunine (2005). Moreover, Housen et al. (1999) found that the craters predominantly formed by
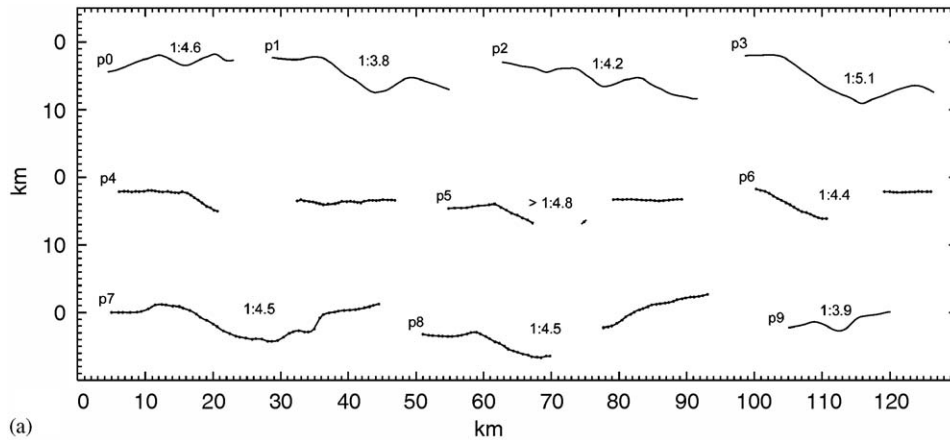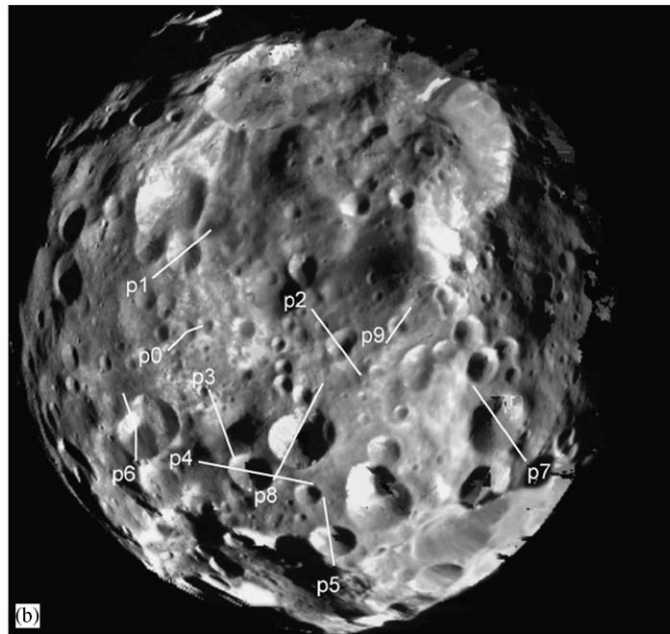
Fig. 9. (a) Profiles showing the morphology of selected craters. Note the conical shape of the craters profiled by p0–p6. The shape of crater #9 is probably not fully resolved by the DTM and therefore may be conical too. Craters #7, 8 seem to be more bowl-shaped but it has to be noted that DTM coverage is poor in these areas (and just one profile could be extracted). (b) Locations of profiles in ortho-image mosaic.

compression rather than excavation of material. This implies that the depth-to-diameter ratio of the craters must increase with lower material compaction and higher porosity (Love et al., 1993). The higher depth-to-diameter ratios for most of the craters on Phoebe as compared to those measured on other small bodies like Phobos, Deimos, Ida, and Eros (Thomas, 1999; Robinson et al., 2002) may thus be related to the presence of lower compaction material on Phoebe.

cant morphologic detail, notably on the morphology of impact craters. Several small craters show high depth-to-diameter ratios and pronounced conical shapes that may hint at the presence of porous, low-compaction material on the surface of Phoebe. On the same lines, there is evidence for unconsolidated material at the eastern rim of Jason crater. While the Cassini mission continues, no new images are expected for Phoebe.

5. Summary

Cassini stereo images have been used to derive a control point network, a spin-axis solution, a DTM and an orthoimage mosaic of Phoebe. The DTM, which covers approximately 1/3 of the satellites surface reveals signifi-
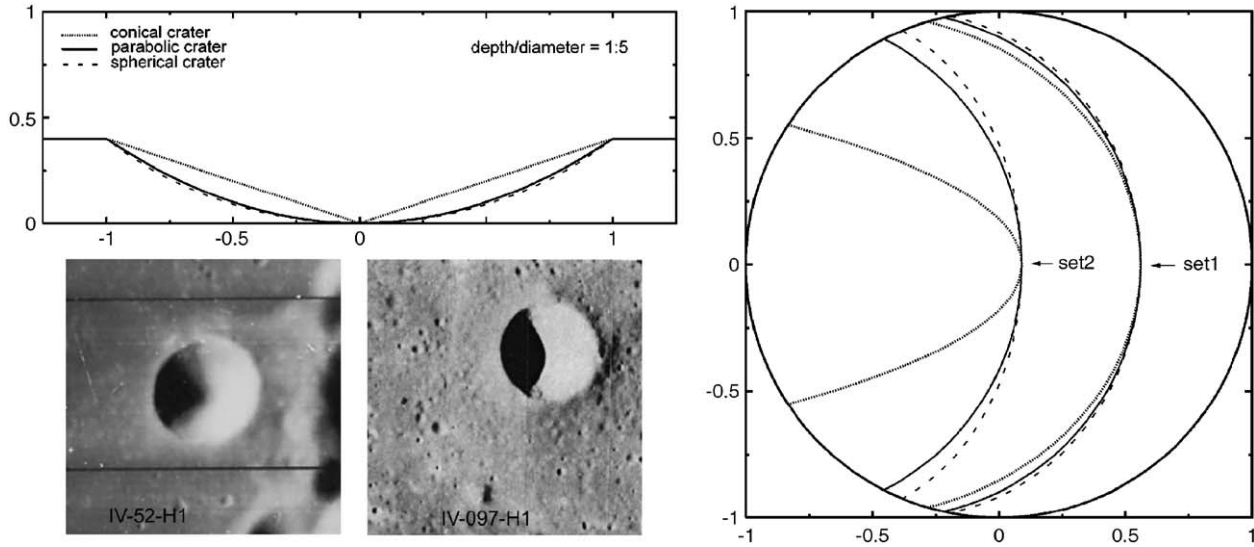
Acknowledgement

Fig. 10. Simulated shadow contours for different crater shapes and illumination. (Top left) Sketch of studied crater forms. Bowl-shaped craters are modeled by a parabola-like and a spherical shape, respectively. (Right) Two sets of shadow contours resulting from different Sun elevations. While at low incidence angle (set1) there are very similar shadow contours of the three crater shapes, higher incidence angles (set2) result in distinctive silhouettes: conical craters exhibit narrow parabolic shadow contours (dotted line) and bowl-shaped craters show more circular shadow cones. (Bottom left) Lunar mare craters showing shadow contours consistent with a conical crater (left) and a bowl-shaped crater (right). Both craters have diameters of ∼8 km.The lunar conical crater well compares to crater #1 of Phoebe (Fig. 5).

Appendix

From the global shape model, Phoebe can roughly be approximated by a sphere of ∼107 km radius (Porco et al., 2005). Here, we evaluate the impact of a non-spherical mass accumulation (topographic anomaly) on heights and slopes.

Significant deviations from spherical heights and slopes are to be expected at the eastern rim of Jason (Fig. 4), which represents a major topographic anomaly. To simplify the problem, we consider two homogeneous spheres S_i (radius R_i, mass M_i, $i = 1,2$) of equal density in rotation, as shown in Fig. 11. The deviations from spherical heights and slopes can be evaluated from the run of the equipotential lines relative to S_1. The geo-potential U_{geo} at a point $r(x,y,z)$ is the sum of the rotation potential and the gravity potentials of the spheres. The rotation potential at a rate ω is given by

$$U_{rot} = -\frac{\omega^2}{2}\left(x^2 + y^2\right),$$

and the gravity potential of each sphere is given by

$$U_{grav,i} = -\frac{G\,M_i}{|r - r_{0,i}|}, \text{ if } |r - r_{0,i}| \geqslant R_i, \text{ and}$$

$$U_{grav,i} = -\frac{G\,M_i}{|r - r_{0,i}|}\left[\frac{3}{2} - \frac{1}{2}\left(\frac{|r - r_{0,i}|}{R_i}\right)^2\right] \text{ otherwise.}$$

Here, G is the constant of gravity and $r_{0,i}$ is the position of the center of the sphere.

Equipotential lines meet the equation

$$U_{geo}(x,y,z) = \text{const.} \tag{1}$$

Scaling by $(G\,M_1)/R_1$ this equation only depends on the ratio of the rotation potential to the gravity potential of S_1 given by $q = \omega^2 R_1^3/G\,M_1$ and the diameter ratio D_2/D_1.

Using spherical coordinates (r,ϑ,φ) Eq. (1) can be solved numerically for $r = r(\vartheta)$ at $\varphi = 0°, 180°$ (EPL in x–z-plane), and for $r = r(\varphi)$ at $\vartheta = 90°$ (EPL in x–y-plane) (Fig. 11).

The general result shown by Fig. 11 is that the equipotential lines are in line with the trend of topography and thus lead to smaller heights and slopes towards the topographic anomaly as compared to those measured with respect to the spherical reference surface. Rotation of the body still enhances this effect. For a plane sphere rotation is only important for slopes over scales comparable to or larger than the radius of the sphere. In particular, for Phoebe's rotational rate (9.3 h) and a diameter ratio D_2/D_1 of 1/5, which was taken so as to model the topography of the eastern rim section of Jason, we obtain a maximum reduction of 7° for slopes measured along the equator of S_1 towards S_2 and of 8° for slopes measured from the poles of S_1 towards S_2 (Fig. 11, top). The range of impact on heights and slopes extends over about $1.5D_2$ measured from the center of S_2. Topographic anomalies with diameters $D_2 \leqslant 1/10 D_1$ do not change slopes significantly and can be neglected (Fig. 11, bottom).

In summary, close to the eastern rim of Jason slopes measured relative to a spherical reference are likely too steep by about 7–8° but at distances of ∼100 km and over scales smaller than Phoebe's radius slopes are expected to
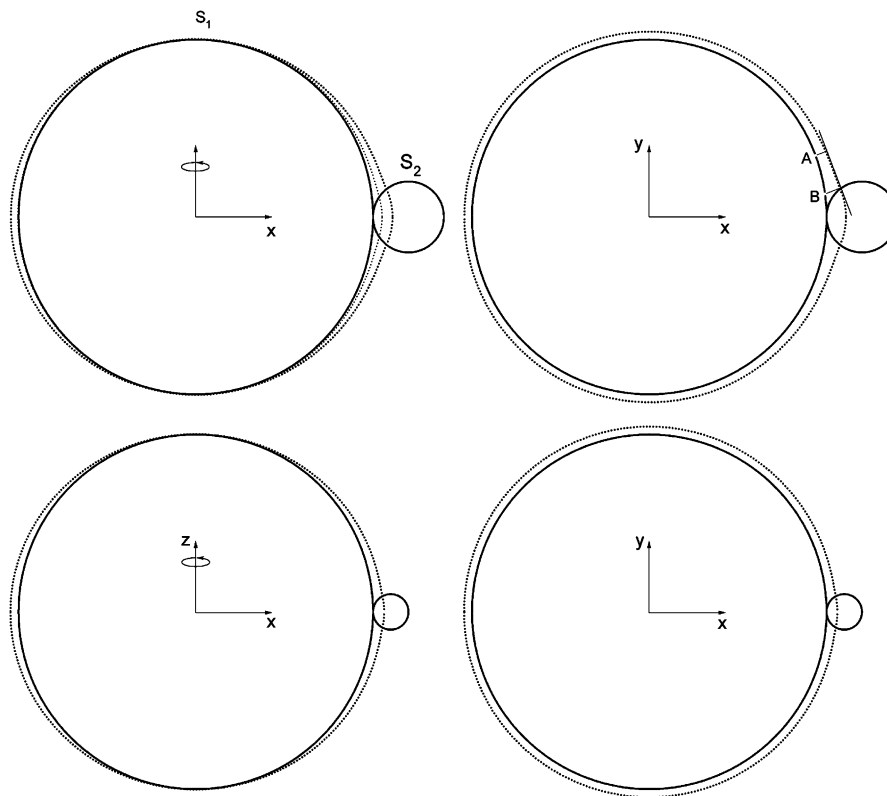
Fig. 11. Sketch of the considered model. Two spheres are in rotation about the z-axis with the smaller sphere (S_2) representing the rim topography of Jason (which is located close to the equator). Equipotential lines (EPLs) are shown for $q = 0.078$ (appropriate to Phoebe) and $D_2/D_1 = 0.2$ (top) and $D_2/D_1 = 0.1$ (bottom). (Left) EPLs in x–z plane. (Right) EPLs in the x–y plane. (Top left) shows the impact of rotation. Dotted line next to the surface of S_1 is for $q = 0$ (no rotation). (Top right) While there is no slope from point A to point B when their heights are measured relative to the surface of S_1 there is a slope of $-7°$ when the heights are measured relative to the equipotential surface (dotted line).

be reliable within 1–$2°$. Although the considered model is simple as compared to the observed rim topography of Jason it shows the basic effects of topography and rotation on heights and slopes. The obtained maximum correction of $8°$ is significant for slope-related studies but it has to be stressed that it is an upper limit just reached close to the eastern rim of Jason. Also, even with this maximum correction morphologic features do not change dramatically as a comparison between measured and model-corrected slopes shows (Fig. 6).

References

Bauer, J.M., Buratti, B.J., Simonelli, D.P., Owen, W.M., 2004. Recovering the rotational Lightcurve of Phoebe. Astrophys. J. 610, L57.

Colvin, T.R., Davies, M.E., Rogers, P.G., Heller, J., 1989. NASA STI/Recon Technical Report N-2934-NASA.

Cuk, M., Burns, J.A., 2004. Gas-drag-assisted capture of Himalia's family. Icarus 167, 369–381.

Giese, B., Oberst, J., Roatsch, T., Neukum, G., Head, J.W., Pappalardo, R.T., 1998. The local topography of Uruk Sulcus and Galileo Regio obtained from stereo images. Icarus 135, 303–316.

Herrmann, H.J., 2002. Granular matter. Physica A 313, 188–210.

Housen, K.R., Holsapple, K.A., Voss, M.E., 1999. Compaction as the origin of unusual craters on asteroid Mathilde. Nature 402, 155–157.

Johnson, T.V., Lunine, J., 2005. Saturn's moon Phoebe as a captured body from the outer Solar system. Nature 435, 69–71.

Love, S.G., Hörz, F., Brownlee, D., 1993. Target porosity effects in impact cratering and collisional disruption. Icarus 105, 216–224.

Piekutowski, A., 1977. Cratering mechanisms observed in laboratory-scale high-explosive experiments. In: Roddy, D.J., Pepin, R.O., Merrill, R.B. (Eds.), Impact and Explosion Cratering. Pergamon Press, New York, pp. 67–102.

Pollack, J.B., Burns, J.A., Tauber, M.E., 1979. Gas drag in primordial circumplanetary envelopes: a mechanism for satellite capture. Icarus 37, 587–611.

Porco, C.C., 19 colleagues, 2004. Cassini imaging science: instrument characteristics and anticipated scientific investigations at Saturn. Space Sci. Rev. 115, 363–497.

Porco, C.C., 34 colleagues, 2005. Cassini imaging science: initial results on phoebe and iapetus. Science 307, 1237–1242.

Roatsch, Th., Wählisch, M., Scholten, F., Hoffmeister, A., Matz, K-D., Denk, T., Neukum, G., Thomas, P., Helfenstein, P., Porco, C., 2006. Mapping of the icy Saturnian satellites: first results from Cassini-ISS. Planet Space Sci., this issue, doi:10.1016/j.pss.2006.05.032.

Robinson, D.A., Friedman, S.P., 2002. Observations of the effects of particle shape and particle size distribution on avalanching of granular media. Physica A 311, 97–110.

Robinson, M.S., Thomas, P.C., Veverka, J., Murchie, S.L., Wilcox, B.B., 2002. The geology of 433 Eros. Meteorit. Planet. Sci. 37, 1651–1684.

Thomas, P., Veverka, J., Dermott, S., 1986. Satellites. In: Burns, J.A., Matthews, M.S. (Eds.). University of Arizona Press, Tucson, pp. 802–835.

Thomas, P.C., 1989. The shapes of small satellites. Icarus 77, 248–274.

Thomas, P.C., 1993. Gravity, tides, and topography on small satellites and asteroids: application to surface features of the martian satellites. Icarus 105, 326–344.

Thomas, P.C., 1999. Large craters on small objects: occurrence, morphology, and effects. Icarus 142, 89–96.

Wewel, F., 1996. Determination of conjugate points of stereoscopic three line scanner data of Mars 96 mission. Int. Arch. Photogram. Remote Sensing XXXI (B3), 936–939.

Zhou, Y.C., Xu, B.H., Yu, A.B., Zulli, P., 2002. An experimental and numerical study of the angle of repose of coarse spheres. Powder Technol. 125, 45–54.